

# Directional artificial fluid properties for compressible large-eddy simulation



Britton J. Olson <sup>\*</sup>, Sanjiva K. Lele

Department of Aeronautics and Astronautics, Stanford University, 435 Lomita Hall, Stanford, CA 94305, United States

## ARTICLE INFO

### Article history:

Received 11 July 2012

Received in revised form 14 March 2013

Accepted 16 March 2013

Available online 28 March 2013

### Keywords:

Shock waves

Compressible flow

Shock capturing

Large-eddy simulation

Turbulent boundary layer

## ABSTRACT

An improved methodology for large-eddy simulation (LES) for flows involving shock waves and turbulence is described. This approach provides better shock capturing and enhanced resolution of turbulence while preserving numerical stability on high aspect ratio (AR) grids. The proposed improvements are based on the LES approach which uses artificial fluid diffusivities (shear viscosity, bulk viscosity and thermal diffusivity) to damp the unresolved gradients of turbulence, shock waves and contact discontinuities, respectively. The scalar artificial viscosities are active only in under-resolved regions of the flow and added directly to the physical quantities. On high aspect ratio grids, the length scale disparity of the mesh leads to over dissipation in one or more direction, causing mis-prediction of physical quantities and added numerical stiffness which reduces the stable time step by a factor of 1/AR. Our proposed method allows fluid diffusivities to be independently applied along each grid direction by forming directional quantities, which ensure the method is minimally dissipative. This alternative approach reduces the errors and numerical stiffness associated with over dissipation. Several test cases are presented which demonstrate the improved performance of this approach on high aspect ratio grids and the enhanced numerical stability. Brief results from LES of an over-expanded planar nozzle are given which demonstrate the method's robustness on practical applications.

Published by Elsevier Inc.

## 1. Introduction

The complex interaction between shock waves and turbulence poses a long-standing challenge in numerical simulation of compressible fluid dynamics. Spurious oscillations can form near the shock when the numerical method attempts to differentiate a discontinuous function. These spurious waves can severely degrade the quality of the solution and therefore should be damped. However, damping out physical oscillations, such as those associated with turbulence, also leads to incorrect results. Therefore, numerical methods must selectively smear the shock waves so they can be captured without producing ringing, while preserving the physical high wavenumber oscillations in the turbulent field. Furthermore, in an LES approach, only the larger scales or eddies are resolved. For the unresolved scales, a sub-grid scale (SGS) model is used (either explicitly or implicitly) to damp out the oscillations associated with the scales of motion which cannot be supported by the grid. This damping not only serves as an SGS model, but also stabilizes the numerical solution which can grow unstable from the unresolved wavenumbers on the LES grid.

The literature is rich with studies and numerical methods which address the simulation of compressible flows in the context of LES and DNS (c.f. Ref. [1]). High-order central differencing schemes provide excellent resolution of turbulent structures and apply minimal dissipation when compared to other differencing schemes. When shocks are present, however,

\* Corresponding author. Tel.: +1 925 423 6165.

E-mail addresses: [britton.olson@gmail.com](mailto:britton.olson@gmail.com), [olson45@llnl.gov](mailto:olson45@llnl.gov) (B.J. Olson).

the method requires explicit dissipation to smear out discontinuities and avoid numerical ringing. The method of artificial fluid properties applies artificial diffusivities (or fluid properties) in regions of the flow field where there is a lack of resolution or where physical gradients are not resolved by the computational mesh. The artificial diffusivities in these regions are then simply added to the physical ones. This methodology is based on the idea introduced by von Neumann and Richtmyer [2] who added a “non-linear viscosity” to numerically capture a hydrodynamic shock. Jameson et al. [3] added numerical viscosities to the Euler equations to capture shocks and stabilize the numerical solution. More recently, Cook and Cabot [4] introduced a high wavenumber biased “hyperviscosity” which could be used to better resolve turbulence and capture shock waves by ensuring the dissipation was only active near the Nyquist cutoff frequency,  $\pi/\Delta x$ . This idea evolved [5] to include artificial thermal conductivity and artificial species diffusion for multi-species compressible flows. A general form for these artificial diffusion terms was proposed by Kawai [6] for curvilinear grids. The majority of improvements to the artificial diffusivity method have pertained to the artificial bulk viscosity (ABV or  $\beta^*$ ), which acts as the shock capturing scheme.

Mani et al. [7] proposed that  $\beta^*$  be based on the trace of  $S_{ij}$ , rather than its magnitude, which decreased the excessive dissipation of the acoustic and vortical fields. The Ducros sensor [8] and its modifications were used by Bhagatwala and Lele [9] and Kawai et al. [10] to further improve the localization of  $\beta^*$  and decrease the excessive turbulent dissipation away from the shock. This method has been proven effective on a broad range of problems involving shocks and turbulence [6,11–14] and compares quite well to other state-of-the-art methods [15,1].

All efforts to improve ABV have dealt with the locality of  $\beta^*$ , ensuring that it vanishes rapidly in regions void of shock waves. A problem which these previous studies ignore arises on high aspect ratio grids, such as those used to capture wall bounded flows. When the direction of shock propagation is aligned in the direction of coarse grid spacing, values of  $\beta^*$  will become large, scaling independently of the grid spacing in the fine direction. It will be shown, that the stable time step associated with  $\beta^*$  is reduced by a factor of AR compared to the acoustic limit for explicit time stepping schemes. For LES of wall bounded flows, this cost is prohibitive and ABV is typically used with lower-order implicit time advancement schemes [16,11,14,7,17] which circumvents this numerical stiffness problem.

In contrast to the numerous improvements of ABV, artificial shear viscosity (ASV) has been altered little from its originally proposed form. Artificial shear viscosity was introduced by Cook and Cabot [4] which would act as a subgrid-scale (SGS) model for the unresolved vortical motions. The main requirements for the model, Cook argues [5], are the correct energy transfer rate through the cutoff wavenumber and that the model should be high wavenumber biased. The former is automatically satisfied by the use of positive valued artificial shear viscosity and the latter is achieved by using higher-order derivatives to localize the artificial terms in the vicinity of large gradients.

Kawai et al. generalized the application of  $\mu^*$  and used a direct fourth derivative rather than the original biharmonic operator. They showed that  $\mu^*$  performed similarly to the dynamic Smagorinsky model for isotropic turbulence and wall bounded flows. In both cases, the inclusion of the explicit SGS models (versus no model), led to higher dissipation rates for isotropic decaying turbulence and an under-prediction of the wall shear stress for a compressible turbulent boundary layer. At higher Reynolds numbers,  $\mu^*$  was required to ensure stability for the calculations of Kawai et al. For wall bounded flows, our calculations have also demonstrated a loss of stability as the resolution is decreased or the Reynolds number is increased. It is unclear what the precise conditions of stability are when one considers the physics, numerics and grid resolution of the calculation. Therefore, for a robust and accurate method, one would like to ensure stability by including  $\mu^*$  while minimizing its adverse effect of excessive dissipation.

In this paper, we propose an alternative method for applying artificial fluid diffusivities. In this approach the value of artificial diffusion along each grid direction is independently formed and scaled, ensuring that the dissipation is minimal. We have observed that this directional form of ABV alleviates the numerical stiffness and captures shock waves more crisply on high-aspect ratio grids. Furthermore, the directional form of ASV reduces the excess dissipation of the SGS model in the LES of a compressible turbulent boundary layer.

The paper is divided into two sections; LES methodology and numerical test cases. The methodology (Section 2) gives the equations of motion and introduces a general method for applying the directional ABV to the equations of motion in both Cartesian and generalized coordinates. We suggest a form of the directional ABV that reduces exactly to the scalar form when the grid is isotropic. Directional ASV and artificial thermal conductivity are introduced to the equations of motion and the proposed forms for both are given.

In Section 3, several test cases illustrate the limitations of the scalar form of artificial diffusivity and the observed improvements of the directional form. Simulation of a cylindrical shock wave and a shock boundary layer interaction show the enhancements in stability and shock capturing ability in Sections 3.1 and 3.2. Section 3.3 shows results from an LES of a turbulent boundary layer which shows that the directional form of  $\mu^*$  improves the solution over the scalar case. Finally in Section 3.4, results from an LES of an over-expanded planar nozzle are briefly discussed to show the method’s capability on problems of practical interest.

## 2. Methodology

### 2.1. Governing equations

The compressible Navier–Stokes equations in Cartesian coordinates,  $\mathbf{x} \equiv (x, y, z)$ , can be written in conservative form as follows:

$$\frac{\partial \mathbf{U}}{\partial t} + \nabla_{\mathbf{x}} \cdot \mathbf{F}_{\mathbf{x}} = 0. \quad (1)$$

The conserved variables and flux vectors in the three directions are given by:

$$\begin{aligned} \mathbf{U} &= \begin{pmatrix} \rho \\ \rho u \\ \rho v \\ \rho w \\ E \end{pmatrix}, \quad \mathbf{F}_x = \begin{pmatrix} \rho u \\ \rho u^2 + p - \tau_{xx} \\ \rho uv - \tau_{xy} \\ \rho uw - \tau_{xz} \\ u(E + p - \tau_{xx}) - v\tau_{xy} - w\tau_{xz} - Q_x \end{pmatrix}, \\ \mathbf{F}_y &= \begin{pmatrix} \rho v \\ \rho uv - \tau_{xy} \\ \rho v^2 + p - \tau_{yy} \\ \rho vw - \tau_{yz} \\ v(E + p - \tau_{yy}) - u\tau_{xy} - w\tau_{yz} - Q_y \end{pmatrix} \\ \mathbf{F}_z &= \begin{pmatrix} \rho w \\ \rho uw - \tau_{xz} \\ \rho vw - \tau_{yz} \\ \rho w^2 + p - \tau_{zz} \\ w(E + p - \tau_{zz}) - u\tau_{xz} - v\tau_{yz} - Q_z \end{pmatrix}, \end{aligned}$$

$$\nabla_{\mathbf{x}} \equiv \left( \frac{\partial}{\partial x}, \frac{\partial}{\partial y}, \frac{\partial}{\partial z} \right)$$

where  $\rho, p, u, v, w, E$  are the density, pressure, three components of velocity and total energy respectively. Eq. 1 can be transformed into general curvilinear coordinates [18]  $\xi \equiv (\xi, \eta, \zeta)$  as follows:

$$\frac{\partial \mathbf{U}}{\partial t} + (\nabla_{\xi} \cdot \mathbf{F}_{\xi}) \frac{1}{\det J} = 0, \quad (2)$$

where,

$$\mathbf{F}_{\xi_i} = \mathbf{F}_{x_j} \frac{\partial \xi_i}{\partial x_j} \det J, \quad (3)$$

$$J_{ij} = \frac{\partial \mathbf{x}_i}{\partial \xi_j}, \quad \frac{\partial \xi_i}{\partial x_j} = (J_{ij})^{-1}$$

and

$$\nabla_{\xi} \equiv \left( \frac{\partial}{\partial \xi}, \frac{\partial}{\partial \eta}, \frac{\partial}{\partial \zeta} \right).$$

In either coordinate frame, the viscous stress tensor is given as

$$\tau_{ij} = 2\mu S_{ij} + \left( \beta - \frac{2}{3}\mu \right) S_{kk} \delta_{ij}, \quad (4)$$

where

$$S_{ij} = \frac{1}{2} \left( \frac{\partial u_i}{\partial x_j} + \frac{\partial u_j}{\partial x_i} \right),$$

$$E = \frac{p}{\gamma - 1} + \frac{1}{2} \rho u_i u_i,$$

$$T = \frac{p}{\rho R},$$

$$Q_i = -\kappa \frac{\partial T}{\partial x_i}$$

are the symmetric strain-rate tensor, total energy, temperature and heat flux respectively.

In the Navier-Stokes equations, physical diffusion is present and is set by the shear viscosity ( $\mu$ ), bulk viscosity ( $\beta$ ) and the thermal diffusivity ( $\kappa$ ). Shear viscosity is set by the Reynolds number, thermal diffusivity is set by the Prandtl number and

the physical bulk viscosity is assumed to be zero.  $R$  is the specific ideal gas constant and  $\gamma$  is the ratio of specific heats, taken to be 1.4 for all the calculations herein.

The equations are solved using a 10th-order compact finite difference scheme [19] for spatial differentiation and a five stage 4th-order Runge–Kutta scheme [20] for temporal integration. An 8th-order low pass filter is applied at every sub-step of the integration to ensure numerical stability of the method. Further details of the method are described by Cook [5].

## 2.2. Artificial fluid properties

For compressible flows involving shock waves, numerical treatment of discontinuities is needed to avoid spurious oscillations. For high-order finite difference schemes, the use of artificial diffusivities is an attractive approach to smooth out shock waves, unresolved vortical motion and contact discontinuities. It requires no modification to the differencing method and is easily implemented into existing solvers. It provides a natural way to diffuse shock waves over several grid points by locally increasing the value of bulk viscosity in the vicinity of the shock by adding artificial bulk viscosity ( $\beta^*$ ) to the physical one. Artificial shear viscosity ( $\mu^*$ ) keeps the solution stable in the poorly resolved regions of flow, while providing an SGS model which is biased to high wavenumbers. Artificial thermal conductivity ( $\kappa^*$ ), much like the shock capturing of  $\beta^*$ , acts to diffuse discontinuities in the temperature field. Through numerical experimentation, we found  $\kappa^*$  to be less influential on the overall solution and stability of the simulation than  $\beta^*$  and  $\mu^*$ . Therefore, it will not be the focus of the test cases in Section 3.

Ensuring that the artificial diffusivities are correctly localized and scaled is crucial. Failure to do so will lead to over-dissipation of the flow and damping of the physical oscillations associated with turbulence. Furthermore, increased values of the diffusive terms “stiffen” the equations of motion as they are advanced in time, placing a more stringent constraint on the stable time step.

### 2.2.1. Numerical stiffness on high AR grids

On grids with high-aspect ratios (AR), artificial fluid properties can lead to over-dissipation and numerical stiffness. Fig. 1 shows a structured 2d mesh with  $AR = \Delta_c/\Delta_f$ , where  $\Delta_c$  and  $\Delta_f$  are the coarse and fine local grid spacings. The angle between the shock wave direction of travel and direction of fine grid spacing is defined as  $\theta$ . The length scale over which the shock is smeared, defined as  $\Delta_{\text{Shock}}$ , is therefore dependent on the shock wave orientation,  $\theta$ ; when  $\theta = 0$ ,  $\Delta_{\text{Shock}} \sim \Delta_f$  and when  $\theta = \pi/2$ ,  $\Delta_{\text{Shock}} \sim \Delta_c$ . Artificial bulk viscosity scales as  $\beta^* \sim \rho\delta u\Delta_{\text{Shock}}$  [7], where  $\rho\delta u$  are physical, grid independent quantities across the shock. For numerical stability using an explicit time advancement scheme, the diffusive shock capturing time step size,  $\Delta t$ , must scale as  $\Delta t \sim \rho \frac{\Delta_f^2}{\beta}$ , where  $\Delta_f$  is the smallest grid length scale. In Fig. 1, when  $\theta = 0$  and the shock is aligned in the fine direction ( $\Delta_{\text{Shock}} \sim \Delta_f$ ), the stable time step will scale as  $\Delta t_f \sim \frac{\Delta_f}{\delta u}$ . However, on an identical grid with identical shock Mach number ( $\rho\delta u$  is constant), if the shock is oriented such that  $\theta = \pi/2$  and  $\Delta_{\text{Shock}} \sim \Delta_c$ , the stable time step becomes  $\Delta t_c \sim \frac{1}{\delta u} \frac{\Delta_f^2}{\Delta_c}$  which can be rewritten as  $\Delta t_c = \Delta t_f \frac{1}{AR}$ . The stable time step size has been reduced by a factor of  $1/AR$  due to the shock orientation. For a wall bounded shock boundary layer interaction, where the impinging shock wave orientation is  $\theta = \pi/2$  and the AR of the grid is made large to capture the near wall velocity gradient, the time step size becomes prohibitively small.

This time step restriction can be circumvented by using an implicit time integration scheme near the wall. Doing so typically reduces the order of accuracy of the temporal integration and will produce additional numerical dissipation [10]. The added numerical dissipation leads to decreased resolution of the turbulent boundary layer and under-prediction of the coefficient of friction when compared to explicit time advancement.

## 2.3. Directional artificial bulk viscosity

Therefore, to address the numerical stiffness problem directly, we propose a new directional form for the artificial bulk viscosity which scales and applies artificial dissipation independently in each computational direction. It is added to the equations of motion in the same form as the physical  $\beta$ , through the viscous stress tensor  $\tau_{ij}$  which is now written as:

$$\tau_{ij} = 2\mu S_{ij} + \left( \beta_{ij} + \frac{4}{3}\mu\delta_{ij} \right) S_{kk}, \quad (5)$$

where

$$\beta_{ij} = \beta\delta_{ij} + \beta_{ij}^*, \quad (6)$$

$$\beta_{ij}^* = \frac{\partial\xi_j}{\partial x_i} \beta_{\xi_k}^* \frac{\partial\xi_k}{\partial x_j}^{-1}, \quad (7)$$

$$\beta_{\xi_i}^* = \beta_{\xi_i}^* \delta_{ij} \quad (\text{no sum on } i), \quad (8)$$

$\beta_{\xi_i}^*$  is the directional artificial bulk viscosity in the  $\xi_i$  computational direction,  $\beta$  is the physical bulk viscosity and where  $\delta_{ij}$  is the identity matrix. When  $\beta_{\xi_i}^* = \beta^* \delta_{ij}$  or when the directional artificial viscosities ( $\beta_{\xi_i}^*$ ) are all the same value, the equation for

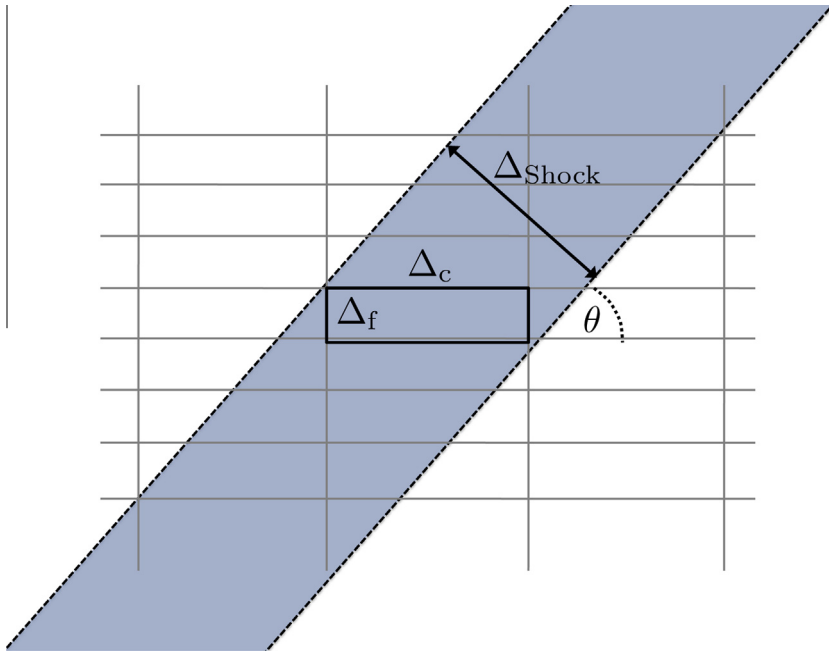


**Fig. 1.** Schematic showing shock alignment on an anisotropic grid. The shock (dotted) is oriented by angle  $\theta$  with respect to lines in the coarse mesh direction. When  $\theta = 0$ ,  $\Delta_{\text{Shock}} \sim \Delta_f$  and when  $\theta = \pi/2$ ,  $\Delta_{\text{Shock}} \sim \Delta_c$ . In either case, artificial bulk viscosity scales as  $\beta^* \sim \rho \delta u \Delta_{\text{Shock}}$ .

$\tau_{ij}$  reduces to exactly to the standard form. Therefore, when forming the quantities  $\beta_{\xi_i}^*$ , it is desirable that they become identical when the grid is isotropic, thereby inheriting the attributes of the scalar form.

A brief note on practical implementation of the proposed method on a finite difference grid is given here. This demonstrates an efficient implementation of the new form of ABV. Furthermore, it is instructive to explicitly show where the artificial terms are added and how that will impact the stability of the solution. The transformed flux can be decomposed to into a physical part (superscript  $P$ ) and an artificial part (superscript  $A$ ) as:

$$\mathbf{F}_{\xi_i} = \mathbf{F}_{\xi_i}^P + \mathbf{F}_{\xi_i}^A. \quad (9)$$

The physical part is calculated as before, using only physical, scalar values for diffusion terms. The numerical portion contains the directional artificial bulk viscosity terms which appear in  $\mathbf{F}_{\xi_i}^A$  through  $\tau_{ij}$  (Eq. (5)) and for the given transformation (Eq. (3)), reduces exactly to:

$$\mathbf{F}_{\xi_i}^A = - \begin{pmatrix} 0 \\ \beta_{\xi_i}^* S_{kk} \left( \frac{\partial \xi_i}{\partial x} \det J \right) \\ \beta_{\xi_i}^* S_{kk} \left( \frac{\partial \xi_i}{\partial y} \det J \right) \\ \beta_{\xi_i}^* S_{kk} \left( \frac{\partial \xi_i}{\partial z} \det J \right) \\ \beta_{\xi_i}^* S_{kk} u_j \left( \frac{\partial \xi_i}{\partial x_j} \det J \right) \end{pmatrix} \quad \text{for } i = 1, 2, 3, \quad (10)$$

where repeated indices imply summation.

It is important to point out that the computational flux terms in each grid direction are only dependent on the directional artificial bulk viscosity in that direction. Since derivatives are computed along these directions, discontinuities in these directions will cause numerical ringing. Therefore, numerical dissipation should be scaled and applied directly to each computational grid direction to ensure that over-dissipation due to large aspect ratios does not occur. Furthermore, in practice, the above method is an efficient way to implement the directional ABV in an existing solver.

The independent application of artificial viscosity along each computational grid direction, bears some resemblance to other shock capturing schemes. For example, WENO and JST schemes [21,3] form artificial fluxes using operators which only depend on a particular coordinate direction. The non-linearity of these differential operators adds numerical diffusion, implicitly, to each computational grid direction. These one-dimensional operators allow the shock wave to be captured cleanly over very few grid points.

Comparisons between WENO, ABV and others were made by Johnson et al. [15] who showed that the WENO method could capture shocks more cleanly than ABV. However, Johnson states that the standard WENO method is “not suitable

for high-fidelity computations of compressible turbulence”, citing its overly dissipative behavior in regions of turbulence. Hybridization and shock sensors are therefore required if the method (WENO, etc.) is to be viable for compressible LES [15]. Unlike WENO, directional ABV maintains the usage of differential operators with zero numerical diffusion. However, similar to WENO, the explicit numerical diffusion is based independently along each of the grid directions. Both methods add numerical diffusion along each grid direction; WENO does so implicitly while directional ABV does so explicitly.

A framework to apply grid direction dependent values of artificial bulk viscosity has been given, but  $\beta_{\xi_i}^*$  has yet to be defined. In the case where  $\beta_{\xi_i} = \beta^*$ , the equations are exactly consistant with the standard scalar form. As mentioned before, this is a desirable attribute in selecting  $\beta_{\xi_i}^*$  as doing so will ensure the method inherits the positive attributes demonstrated in previous studies [5,7,6,10,9].

Enforcing the aforementioned constraint, we modify a recently proposed form for scalar  $\beta^*$  from Kawai et al. [10] to be:

$$\beta_{\xi_i}^* = C_\beta \rho \left( \sum_{j=1}^3 \overline{\left| \frac{\partial^4 (S_{kk})}{\partial \xi_j^4} \right|} \Delta \xi_j^4 \Delta L_{\xi_j} \right) \Delta L_{\xi_i}, \quad i = 1, 2, 3, \quad (11)$$

where  $\Delta \xi_i$  is the computational grid length scale and  $\Delta L_{\xi_i}$  and  $\Delta L_{\xi_j}$  are physical length scales of the grid in each computational direction computed as:

$$\Delta L_{\xi_i} = \sqrt{\sum_{j=1}^3 \left( \frac{\partial x_j}{\partial \xi_i} \Delta \xi_i \right)^2}, \quad i = 1, 2, 3,$$

$$\Delta L_{\xi_i} = \frac{\frac{\partial \rho}{\partial \xi_i} \Delta L_{\xi_i}}{\sqrt{\sum_j \left( \frac{\partial \rho}{\partial \xi_j} \right)^2}}, \quad i = 1, 2, 3.$$

Eq. (11) differs from that of Kawai et al. in that it replaces the square of the density aligned transformed grid spacing,  $\Delta L_{\xi_i}$ , with the product of the density aligned transformed grid spacing and the transformed grid spacing,  $\Delta L_{\xi_i}$ . The overbar in Eq. (11) denotes a Gaussian filter [5] used to eliminate sharp gradients introduced by the absolute value operator and the constant,  $C_\beta$  is 1.0. This form becomes exactly a scalar when  $\Delta L_{\xi} = \Delta L_\eta = \Delta L_\zeta$  or when the grid is isotropic.

The proposed directional ABV alleviates the numerical stiffness since  $\beta_{\xi_i}^*$  now scales independently in each direction. The minimum time step between the inviscid Courant–Friedrichs–Lewy (CFL) condition [18] and the diffusive limit dictates the stable time step size. For the scalar form of ABV, when  $\theta = \pi/2$  on a wall bounded flow with  $AR > M_\infty + 1$  this expression can be approximated by

$$\Delta t \sim \frac{\Delta f}{c_\infty} \min \left( \text{CFL}, \frac{c_\infty}{\delta u} \frac{1}{AR} \right),$$

where CFL is the Courant–Friedrichs–Lewy stability limit (typically near unity for explicit time integration) and where the diffusive time step limit is  $\Delta t \sim \frac{\rho \Delta f^2}{\beta^*}$  with  $\beta^* \sim \rho \delta u \Delta_c$ , as before. In this approximation,  $M_\infty$  and  $c_\infty$  are the free stream Mach number and sound speed, respectively. For a directional bulk viscosity implementation, we allow the terms to scale independently of the other grid directions. Doing so gives a new scaling for the maximum stable time step as,

$$\Delta t \sim \frac{\Delta f}{c_\infty} \min \left( \text{CFL}, \frac{c_\infty}{\delta u} \right),$$

where now  $\Delta t_\beta \sim \frac{\rho \Delta f^2}{\beta_{\xi_i}^*}$  and  $\beta_{\xi_i}^* \sim \rho \delta u \Delta_{\xi_i}$ . Note the time step is now only dependent on physical quantities and the smallest grid direction. For the test cases in this paper with shock Mach number less than 3,  $c_\infty/\delta u > 1$ , meaning the simulation was always stable at the convective limit with a CFL of 1. Although the above analysis only gives an approximation to the stable time step scaling for a single problem, it will be shown to hold in practice in Section 3 through numerical experimentation.

#### 2.4. Directional artificial shear viscosity and thermal diffusivity

In a similar fashion, artificial shear viscosity ( $\mu^*$ ) and artificial thermal diffusivity ( $\kappa^*$ ) can be formed as directional quantities as in Eqs. (6)–(8). Artificial fluxes can be constructed which are then added to the physical ones before the derivative operators are applied. As before, the artificial fluxes are dependent only on their corresponding directional artificial diffusion term. Although numerical stiffness was less of an issue with  $\mu^*$  and  $\kappa^*$  (harsh time steps only arose on very high AR grids, where  $AR > 50$ ), the directional form will reduce the numerical dissipation for high aspect ratio grids which leads to a reduction in numerical error. The proposed form for  $\mu_{\xi_i}^*$  and  $\kappa_{\xi_i}^*$  are taken from their most recent enhancement [10] and given as,

$$\mu_{\xi_i}^* = C_\mu \rho \overline{\left| \frac{\partial^4 \mathbf{S}}{\partial \xi_i^4} \right|} \Delta \xi_i^4 \Delta L_{\xi_i}^2, \quad i = 1, 2, 3, \quad (12)$$

$$\kappa_{\xi_i}^* = C_\kappa \rho \frac{c_s}{T} \left( \sum_{j=1}^3 \left| \frac{\partial^4 e}{\partial \xi_j^4} \right| \Delta L_{\xi_i} \right), \quad i = 1, 2, 3, \quad (13)$$

where  $\mathbf{S} = \sqrt{S_{ij}S_{ji}}$  is the magnitude of the strain rate tensor,  $c_s$  is the local sound speed and  $e = \frac{1}{\gamma-1} \frac{p}{\rho}$  is the internal energy of the gas. Unless otherwise specified the coefficients,  $C_\mu$  and  $C_\kappa$  were 0.002 and 0.1 respectively.

### 3. Numerical test cases

#### 3.1. 2D blast wave on an anisotropic grid

A robust shock capturing scheme should accurately capture shock waves which are arbitrarily aligned with the computational mesh. Furthermore, the method ought to maintain this capability over a range of aspect ratios. A simple test case which efficiently tests the aforementioned attributes is the propagation of a cylindrical shock wave on an anisotropic grid. All shock orientations are present simultaneously and therefore can readily reveal dissipation errors and numerical stiffness which are dependent of shock orientation. This test case will demonstrate the enhanced shock capturing ability and added numerical stability of directional bulk viscosity. A pressure field is initialized with a Gaussian distribution whose peak value is large enough to cause the formation of a shock. The primitive variables are initialized as follows:

$$\begin{aligned} p &= p_0 \left( 1 + (P_g - 1) e^{-(R/\delta_g)^2} \right), \\ \rho &= \rho_0 \left( \frac{p}{p_0} \right)^{1/\gamma}, \\ u &= v = 0, \end{aligned}$$

where,  $R^2 = (x - x_c)^2 + (y - y_c)^2$ ,  $x$  &  $y \in [0, L]$ ,  $L = 1$ ,  $p_0 = 1$ ,  $\rho_0 = \gamma$ ,  $\gamma = 1.4$ ,  $P_g = 10$ ,  $\delta_g = 0.05$  and  $x_c = y_c = 0.5$ . For all cases, the solution at time  $t = .25L/c_0$  is compared, where  $c_0$  is the ambient sound speed. Fig. 2 shows 16 contours of pressure, evenly spaced between 1.2 and 1.8 for an aspect ratio of 32. From Fig. 2, two notable improvements over the scalar  $\beta^*$  are observable. First, when the shock is aligned in the coarse direction (or when  $\theta = 90^\circ$ ), the expansion fan immediately after the shock accumulates errors which are evidenced by the non-isotropic spacing of pressure contour lines. For the directional bulk viscosity, errors in the expansion region are noticeably improved. Pressure profiles indicate that the shock location is independent of  $\theta$  and choice of artificial bulk viscosity.

Another difference is apparent when the shock is aligned with the fine direction or when  $\theta = 0^\circ$ . One can see that the shock is much sharper for the directional bulk viscosity case versus the scalar bulk viscosity case. The shock thickness can be approximated by comparing values of divergence ( $\nabla \cdot \mathbf{u}$ ) across the shock. Since the Mach number of the shock is constant for all cases and orientations, the change in velocity across the shock is also constant at a given physical time. Therefore, if a shock is captured over the same number of grid points, the quantity  $\max(-\nabla \cdot \mathbf{u})_\theta \Delta_\theta$  will remain constant, where the subscript denotes values taken along directions of constant  $\theta$ . Normalizing by the value of this product on an isotropic grid ( $AR = 1$ ) gives the non-dimensional shock thickness as:

$$\tilde{\Delta}_{S,\theta} = \frac{\max(-\nabla \cdot \mathbf{u})_{AR=1} \Delta_{AR=1}}{\max(-\nabla \cdot \mathbf{u})_\theta \Delta_\theta}. \quad (14)$$

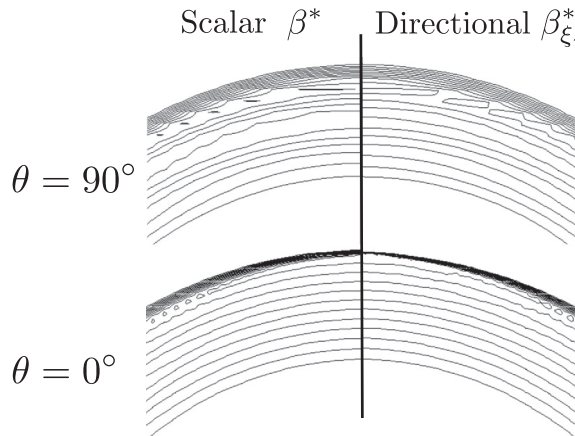


**Fig. 2.** Comparison between the scalar  $\beta^*$  and the proposed directional  $\beta_{\xi_i}^*$  for the cylindrical shock wave case at aspect ratio of 32. Shock is captured more sharply for  $\theta = 0^\circ$  and with less errors in the region immediately behind the shock for  $\theta = 90^\circ$ .

**Table 1**

Table of stable time step size (given in acoustic CFL limit units) and the numerical shock thickness (Eq. (14)) for the cylindrical shock wave case for different aspect ratios (AR). Values for CFL and the normalized shock thickness are within  $\pm 0.1$  and  $\pm 0.01$  respectively. Normalized shock thickness in the coarse direction ( $\theta = 90^\circ$ ) was effectively uniform and is not tabulated.

AR	CFL ( $\beta^*$ )	$\bar{\Delta}_{S,0^\circ} (\beta^*)$	CFL ( $\beta_{\xi_i}^*$ )	$\bar{\Delta}_{S,0^\circ} (\beta_{\xi_i}^*)$
1	1	1	1	1
2	1	1.25	1	0.91
4	1	1.39	1	1.03
8	0.5	1.40	1	1.09
16	0.3	4.11	1	1.11
32	0.1	8.11	1	1.19

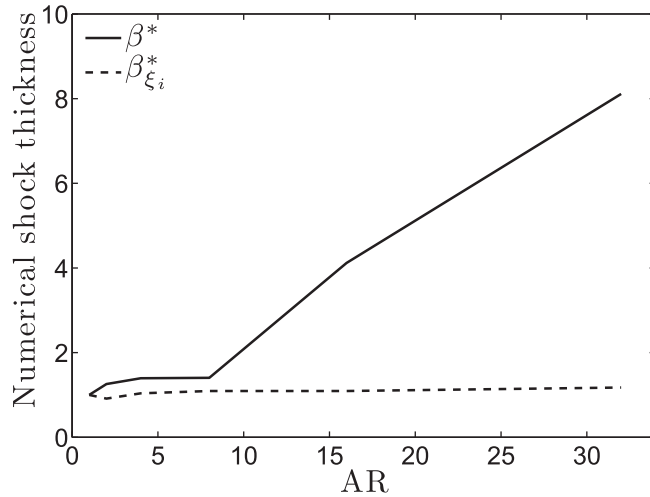


**Fig. 3.** Non-dimensionalized numerical shock wave thickness in the direction of fine mesh spacing ( $\theta = 0^\circ$ ) for the cylindrical blast wave test case. The shock thickness is plotted vs. aspect ratio (AR) for the scalar artificial bulk viscosity  $\beta^*$  (solid) and the directional artificial bulk viscosity  $\beta_{\xi_i}^*$  (dashed) and shows the AR dependence is avoided when the directional form is used.

The non-dimensional shock thickness (Eq. (14)) in the fine direction is given in Table 1 which shows at AR = 32, the scalar bulk viscosity shock is approximately 7 times thicker than for the the directional bulk viscosity. These values are also plotted in Fig. 3 showing the linear relationship with AR.

The more quantifiable justification for using directional bulk viscosity, as previously mentioned, is to alleviate numerical stiffness. This stiffness is illustrated in Table 1 which lists the stable time step in convective CFL units for scalar and directional bulk viscosities over a range of aspect ratios. These values were obtained iteratively by running the simulation at a constant time step. If the simulation ran to  $t = .25L/c_0$  stably, the time step was increased by 0.1 CFL units and re-initialized. If the simulation failed, the last stable value was reported. After the grid exceeded an aspect ratio of 4, the CFL of the stable time step for scalar bulk viscosity decreased linearly with AR. For the directional form, the CFL was unity for all aspect ratios.

### 3.2. Oblique shock wave impinging on a laminar boundary layer

Viscous boundary layers are resolved using a high aspect ratio computational grids near the wall. In a shock boundary layer interaction, shock waves penetrate a portion of the boundary layer and need to be numerically captured when the grid is anisotropic. Therefore, the artificial bulk viscosity needed for shock capturing can potentially cause numerical stiffness in these regions.

This two-dimensional test case illustrates the ability of the proposed method to accurately and efficiently capture shock waves on boundary layer grids. Grid converged results compare favorably to data from Katzer [22] and show the method is accurately capturing the shock wave as well as the laminar boundary layer across the shock. A study of the numerical stability was conducted, which shows that the method alleviates numerical stiffness and leads to larger time steps without the need for an implicit time advancement scheme.

The problem setup is given entirely in Katzer, where an oblique shock wave impinges on a two-dimensional laminar flat plate boundary layer at the point where the Reynolds number based on the boundary layer streamwise length is 30,000. The ratio of specific heats is 1.4, the free stream Mach number is 2.0 and the net pressure rise across the impinging shock and its reflection is 1.4. The full computational domain is shown in Fig. 4 which shows contours of Mach number and pressure for

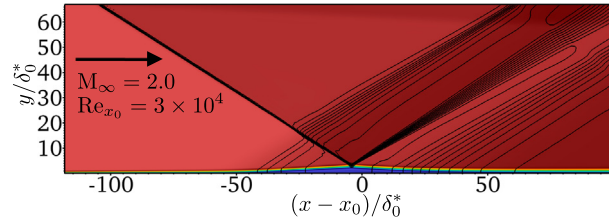


**Fig. 4.** Contours of Mach number range from 0 to 2.0 (blue to red) for the two dimensional shock boundary layer interaction. 16 equally spaced pressure contours (black) between  $1.1p_1$  and  $1.4p_1$  are shown on the fine mesh ( $300 \times 200$ ) using the directional bulk viscosity formulation,  $\beta_{\zeta_i}^*$ . (For interpretation of the references to color in this figure legend, the reader is referred to the web version of this article.)

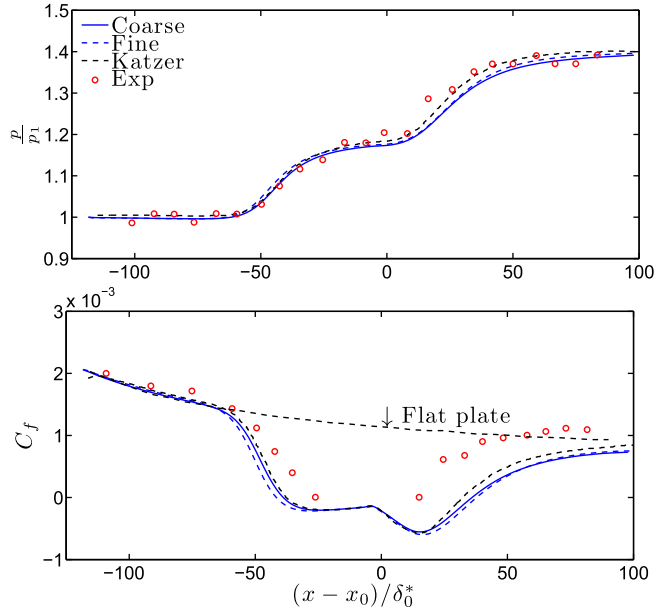


**Fig. 5.** Profiles of wall pressure (top) and skin friction coefficient (bottom), showing comparison with Katzer's calculation [22] (black dashed) and experimental data [23] (red circles) for a shock boundary layer interaction. Blue curves are from the present study for the fine mesh (blue dashed) and coarse mesh (blue solid) using  $\beta_{\zeta_i}^*$ . (For interpretation of the references to color in this figure legend, the reader is referred to the web version of this article.)

the oblique shock reflection. The fine grid used a grid size of  $300 \times 200$  in the streamwise and wall normal directions respectively. The coarse calculation used a grid size of  $150 \times 100$ . Both grids used exponential stretching in  $x$  and  $y$  to cluster points near the shock boundary layer interaction. Fig. 5 shows profiles in the streamwise direction of the wall pressure and skin friction coefficient from the two resolution cases as well as data from Katzer and the experiment of Hakkinen [23].

The calculations were run until the flow achieved steady state or when changes in the solution were negligibly small. This steady solution was then used to reinitialize a calculation which uses scalar bulk viscosity. As in the test case from Section 3.1, the time step was varied incrementally to determine the maximum stable time step between the methods. Depending on the particular mesh, the ratio of stable time step size between directional and scalar artificial viscosity varied between unity and 5.75. On the mesh where no increase in the stable time step size was seen, the shock wave didn't interact in regions of high aspect ratio grid cells. Fig. 6 shows the oblique shock wave visualized by contours of directional ABV in the wall normal direction ( $\beta_{\eta}^*$ ), which becomes negligibly small for  $AR > 4.0$ . On the meshes where the shock wave was present in regions of  $AR > 4$ , numerical stiffness arose.

### 3.3. Large-eddy simulation of a supersonic turbulent boundary layer

Artificial diffusivities are only active when physical gradients are unresolved by the computational mesh. In the previous examples, the physical shock thickness was much smaller than the grid and was smeared using artificial bulk viscosity. However, neither case required artificial shear viscosity to smooth out the physical gradients associated with  $S_{ij}$  as those scales were explicitly resolved. To test the directional artificial shear viscosity, we perform an LES of a supersonic turbulent boundary layer.

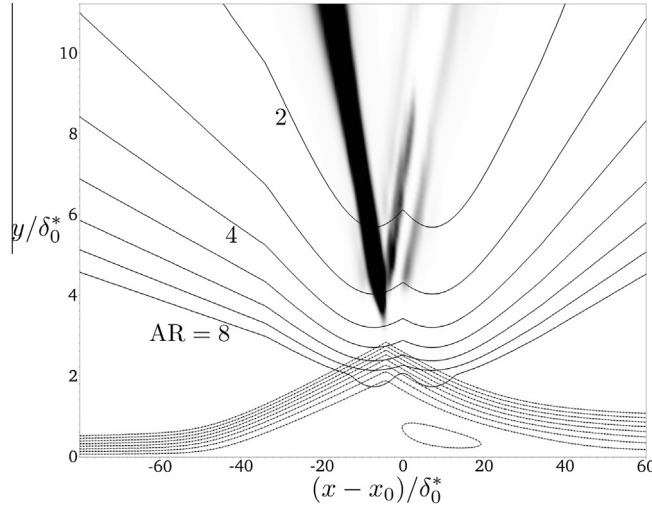


**Fig. 6.** Solid black contour shows peak value of artificial bulk viscosity in the wall normal direction ( $\beta_\eta^*$ ). Black solid lines show contours of the grid aspect ratio and dashed lines show 10 contours of the local Mach number from 0 to 1.0. On this grid, the shock is weak (and hence the artificial bulk viscosity is small) for  $AR > 4.0$ . Therefore, a time step based on a CFL of one, is stable for both the directional and scalar bulk viscosities.

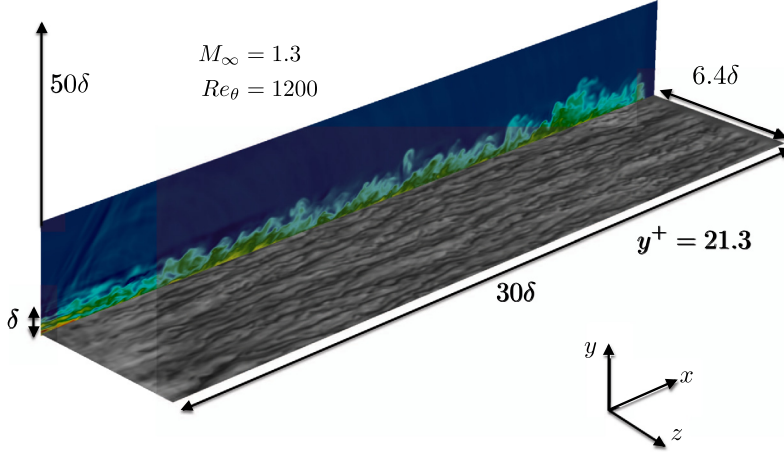


**Fig. 7.** Local temperature contours from blue (.9 $T_\infty$ ) to red (1.5 $T_\infty$ ) on the back plane visualizing the Mach 1.3 turbulent boundary layer. The black and white contours in the  $xz$  plane show instantaneous streamwise velocity contours at  $y^+ = 21.3$ . The domain is given in units of boundary layer thickness ( $\delta$ ) and the Reynolds number based on the momentum thickness ( $\theta$ ) is approximately 1200. (For interpretation of the references to color in this figure legend, the reader is referred to the web version of this article.)

The free stream Mach number is 1.3 and the Reynolds number based on momentum thickness is approximately 1200 at the inlet. These match the conditions from the DNS performed by Pirozzoli et al. [24]. The fine LES used a grid size of  $768 \times 256 \times 128$  mesh points and a domain size of  $30\delta \times 50\delta \times 6.4\delta$  in the streamwise, wall normal and spanwise directions, respectively. With exponential stretching in the wall normal direction, the grid spacing at the wall in viscous units is then  $\Delta x^+ = 12.5$ ,  $\Delta y^+ = 0.8$  and  $\Delta z^+ = 14.7$  in the three directions. For the coarse mesh LES, the grid size was  $512 \times 192 \times 96$  mesh points with near wall grid spacings of  $\Delta x^+ = 18$ ,  $\Delta y^+ = 0.9$  and  $\Delta z^+ = 20.8$  in the three directions. To generate the turbulent boundary layer at the inlet, the method of digital filtering [25] was used which provides fluctuations based on the mean statistics in the boundary layer. For the mean statistics, data from Pirozzoli's DNS were used. After about  $10\delta$  the boundary layer was in equilibrium as evidenced by the stationary coefficient of friction,  $C_f$  (Fig. 10). The two forms of artificial shear viscosity (scalar and directional) were used and compared to the case with no explicit SGS model at the fine mesh resolution (Fig. 8). Results from the coarse and fine mesh LES using directional shear viscosity are given in Fig. 9. Fig. 7 shows a portion of the domain which has been truncated in the wall normal direction and shows contours of instantaneous temperature in the  $xy$  plane and contours of streamwise velocity in the  $xz$  plane.

In addition to its use as an explicit SGS model,  $\mu^*$  also provides numerical stability for unresolved gradients that might otherwise lead to numerical oscillation and instability. However, this is not always the case. In some instances [11,10] arti-

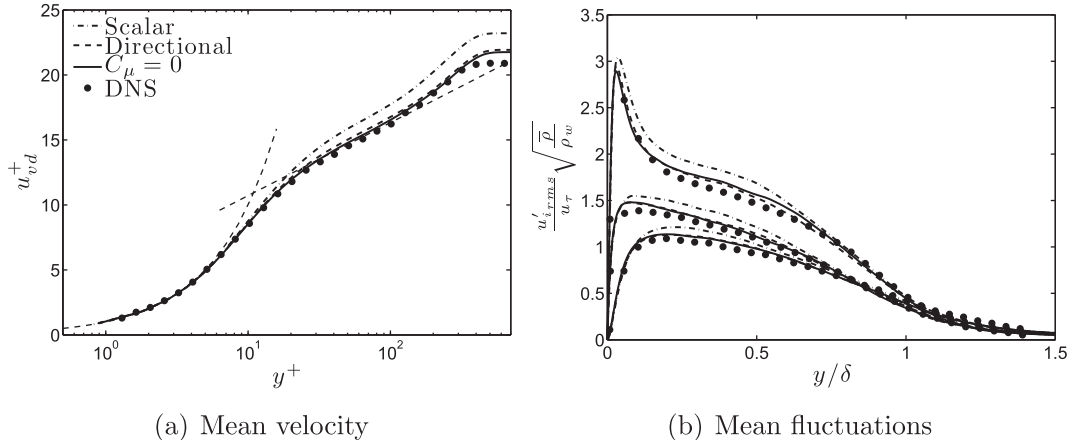


**Fig. 8.** Mean profiles for the Mach 1.3 turbulent boundary layer case at  $x/\delta = 20$ . (Left) Van Driest transformed mean velocity profiles show that the directional artificial shear viscosity and the no artificial shear ( $C_\mu = 0$ ) cases collapse to the log law,  $u^+ = \frac{1}{k} \log y^+ + C$  where  $k = .41$  and  $C = 5.1$ . (Right) Mean profiles of the Reynolds stress components  $u_{rms}$ ,  $w_{rms}$  and  $v_{rms}$  in descending order. For both plots, dashed-dotted denotes scalar ASV, dashed lines are the directional ASV and solid lines are  $C_\mu = 0$ . DNS data (solid circles) from Pirozzoli et al. [24] are plotted for reference.

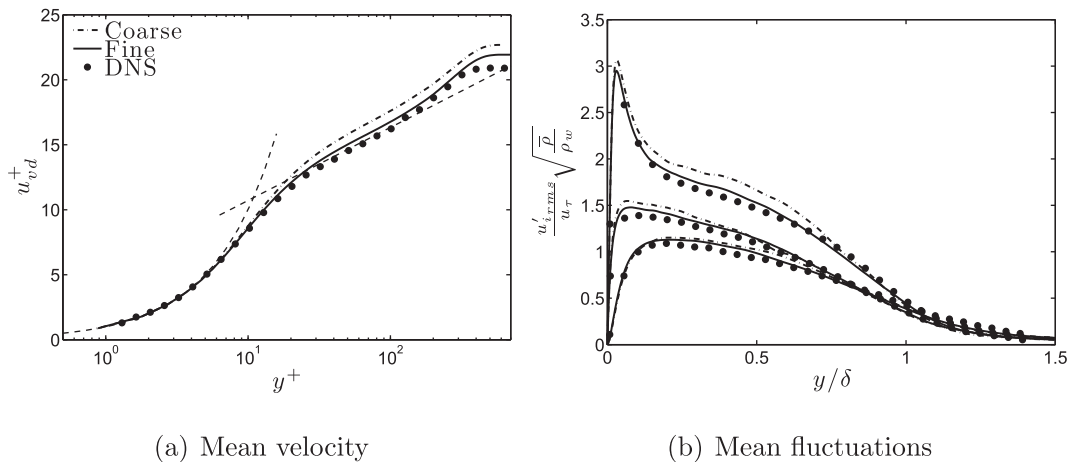


**Fig. 9.** Mean profiles for the Mach 1.3 turbulent boundary layer case at  $x/\delta = 20$  using directional shear viscosity for the LES. (Left) Van Driest transformed mean velocity profiles. (Right) Mean profiles of the Reynolds stress components  $u_{rms}$ ,  $w_{rms}$  and  $v_{rms}$  in descending order. For both plots, dashed-dotted denotes the coarse mesh LES and solid lines are the fine mesh LES. DNS data (solid circles) from Pirozzoli et al. [24] are plotted for reference.

ificial shear viscosity can be turned off and numerical stability is maintained while in others [13,16] shear viscosity is needed for stability. The exact combination of Reynolds number, mesh resolution and numerics (time-stepping, filtering, etc.) which necessitates  $\mu^*$  for stability is unknown, although results from Kawai et al. [10] do indicate that instability usually ensues on coarse LES grids. However, for a general method, one would prefer to toggle as few switches as possible when stability characteristics of a simulation are not known *a priori*. Kawai et al. found that for wall bounded flows, the presence of  $\mu^*$  led to an under prediction of wall shear-stress,  $\tau_w$ , by approximately 5% for their calculations. Hence, when stability is not an issue, one would prefer to turn off artificial shear viscosity.

Directional artificial shear viscosity ensures stability, while adding minimal dissipation to the computation. Three calculations of the turbulent boundary layer were performed which used scalar, directional and no artificial shear viscosity at the fine mesh resolution. In the case with no artificial shear viscosity, stability was not an issue as sufficient grid resolution was present. For coarser grids, we found that without  $\mu^*$  the simulation would become unstable. Mean velocity profiles for the three cases are plotted in Fig. 8 which show that the scalar form under predicts  $\tau_w$  by 12% while the directional form under predicts  $\tau_w$  by only 1.5% when compared to case with no shear. The coarse mesh LES using directional shear viscosity gave results similar to those from the fine mesh LES using the scalar artificial shear viscosity. Fig. 9 shows a comparison between the fine and coarse mesh LES using directional artificial shear viscosity and the reference DNS.

The shift in the log-law profile is caused by the artificial shear viscosity. The scalar  $\mu^*$  is adding more dissipation than the directional form and therefore has a larger adverse effect on the boundary layer profile. These artificial terms are explicitly

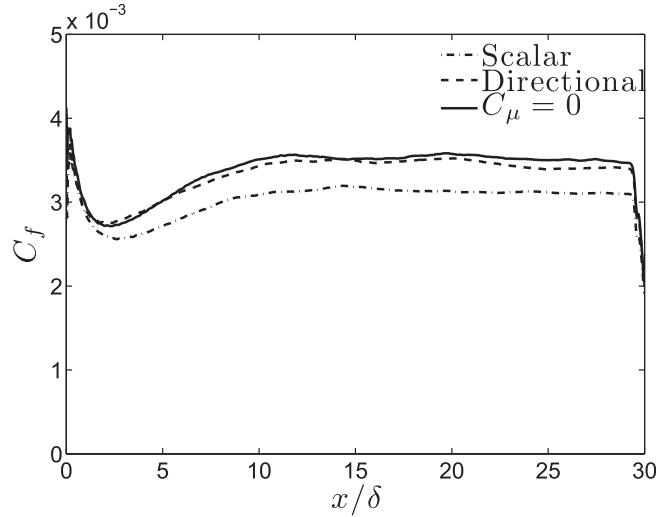


**Fig. 10.** Skin friction coefficient ( $C_f$ ) as a function of  $x/\delta$  for the fine mesh LES. The deviation from the equilibrium at the domain edges is due to the artificial turbulence at the inlet boundary condition and the “sponge” at the outlet boundary.  $C_f$  from the DNS was  $3.9 \times 10^{-3}$ .

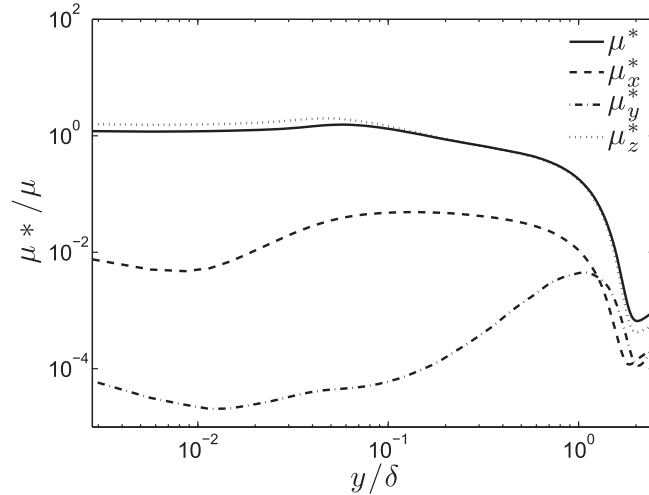


**Fig. 11.** Artificial shear viscosity levels near the wall for the scalar form ( $\mu^*$ ) and the directional form ( $\mu_x^*$ ,  $\mu_y^*$ ,  $\mu_z^*$ ) from the fine mesh LES of the Mach 1.3 turbulent boundary layer.

compared in the boundary layer in Fig. 11 and show that scalar ASV is 4 and 2 orders of magnitude larger than the directional form of ASV in the wall normal ( $\mu_y^*$ ) and streamwise ( $\mu_x^*$ ) directions, respectively. The spanwise component of directional ASV ( $\mu_z^*$ ) is on the same order as the scalar ASV.

### 3.4. Large-eddy simulation of an over-expanded nozzle

Finally, the method is applied to the simulation of a shock boundary layer interaction of practical interest. The full details of this calculation are given by Olson and Lele [13,26]. The geometry is a simple planar diffuser with area ratio (exit area to throat area) of 1.6 and a nozzle pressure ratio (reservoir pressure to ambient pressure) of 1.7. This setup approximates recent experiments by Papamoschou et. al. [27,28]. In this configuration, a turbulent boundary layer interacts with a normal shock wave and separates from the wall, forming a large turbulent shear layer. The shock position is unsteady and oscillates with broadband motion.

LES of this shock boundary layer interaction serves as an excellent “proof of concept” for directional artificial viscosities as it contains turbulence, shocks and high aspect ratio grids. To assess the numerical stiffness, the coarse mesh grid from [13] was analyzed, which had a maximum aspect ratio of 60.86 in the boundary layer portion of the mesh. Aspect ratios are larger in the far field (on account of constant spacing in the spanwise direction) but these regions are neglected in the analysis, as

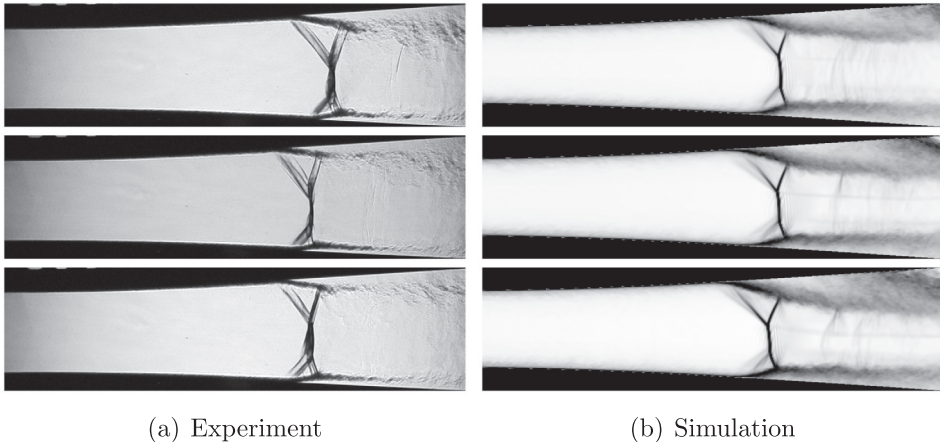


**Fig. 12.** Schlieren images from experiment [28] (left) and z-averaged contours of  $\|\nabla \rho\|$  from the LES (right) show good qualitative agreement of the shock structure, the separated shear layer and the compression/expansion waves.

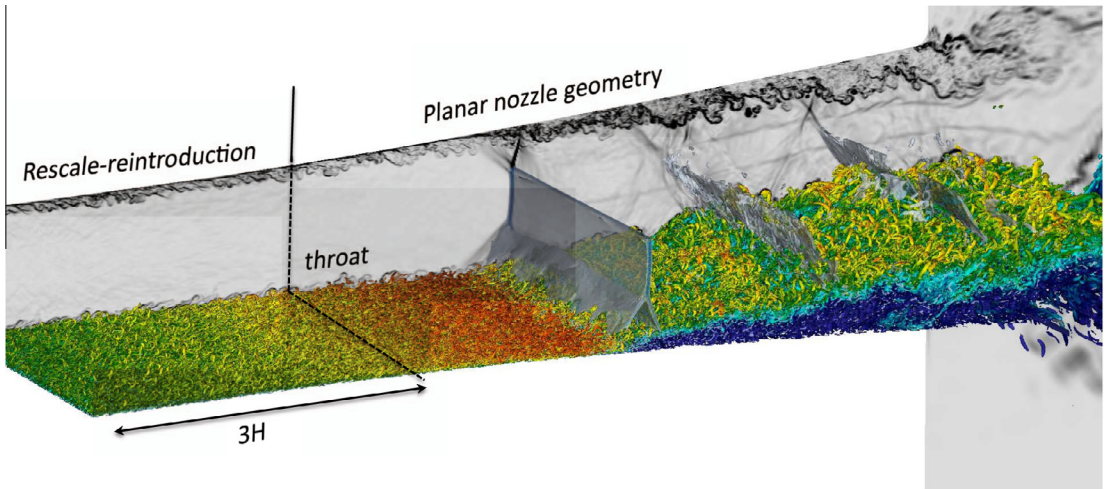


**Fig. 13.** Iso-surface of the Q-criterion [30,31] colored by Mach number show the incoming turbulent boundary layer and the large separated shear layer. The shock is visualized by an iso-surface of  $\nabla \cdot \vec{u}$ . The back plane shows a slice of  $\|\nabla \rho\|$ , depicting the smaller shear layer. The throat location is indicated as is the region which recycles and rescales the incoming turbulent boundary layer. Data are from a fine mesh calculation which used over 150 million grid points.

flow in those regions is very uniform and smooth. Using the directional form, the simulation was run for approximately 3000 time steps at a CFL of 1.0. Then, a restart file was used as an input to a scalar artificial diffusion case and a directional case. The  $\Delta t$  for the time integration was incremented by  $0.025\Delta t_{\text{CFL}}$  and run for 100 time steps, similar to the cylindrical shock test case. If the simulation remained stable (the amplitude of the numerical oscillations did not diverge), the  $\Delta t$  was increased and reinitialized. This process was repeated until the simulation went unstable. Operational stability over a short time horizon is not meant as proof of stability as very small growth rates cannot be excluded.

For the scalar bulk viscosity the largest stable time step was  $\Delta t_{\text{stab}} = [0.1 \pm 0.025]\Delta t_{\text{CFL}}$ . For the directional case,  $\Delta t_{\text{stab}} = [2.18 \pm 0.025]\Delta t_{\text{CFL}}$ . This gives an overall speedup of  $23.32 \pm 6.08$  over the scalar case. Although this test was for an isolated segment of simulation time, it gives a clear picture of the advantages of the method. All LES calculations from Olson and Lele were run at a CFL  $\approx 1.0$  and remained stable for all time.

Fig. 12 shows schlieren images from the experiment and numerical schlieren from the simulation. The simulation captures the two-dimensional, asymmetric shock structure. The incoming turbulent boundary layer is lifted from the wall as it passes through the shock wave and encounters a large pressure gradient. Downstream of the shock, the boundary layer reattaches to the wall on the side which corresponds to the smaller “lambda foot”. On the side with the larger “lambda foot”, the flow forms a large separation region which becomes the source of a low frequency unsteadiness [26,29]. Fig. 13 shows an

instantaneous three-dimensional snapshot of the flow field. An iso-surface of the Q-criterion [30,31] colored by Mach number illustrates the vortical structures in the turbulent boundary layer. An iso-surface of  $\nabla \cdot \mathbf{u}$  in blue shows the shock structure and weak compression waves downstream of the main shock. The black and white back plane are contours of density gradient magnitude, showing the smaller shear layer and the slip lines in the core jet downstream of the main shock.

#### 4. Conclusion

The use of artificial fluid properties for large-eddy simulation of compressible flows is an attractive LES method for high-order finite difference codes. On high aspect ratio grids, the use of the scalar  $\beta^*$  as a shock capturing method becomes problematic, as doing so can lead to prohibitively small time steps. The scalar form of  $\mu^*$  can also be over dissipative and lead to under-prediction of the wall shear stress for turbulent boundary layers. We have proposed a modification to the method, which allows the artificial fluid properties to be not only inhomogeneous in space, but also anisotropic by introducing a directional form. The test cases show that numerical stiffness is alleviated by the directional approach and the shock capturing is enhanced on high aspect ratio grids. Errors in the wall shear stress were reduced by an order of magnitude by using the directional form of artificial shear viscosity for a Mach 1.3 turbulent boundary layer. LES of a supersonic diffuser demonstrated large increases in the throughput of the simulation by increasing the stable time step by over a factor of 20.

#### Acknowledgments

Support for this research was provided by the Department of Energy Computational Science Graduate Fellowship (CSGF). We wish to thank Dr. Andrew Cook and Dr. William Cabot for use of their code and for many valuable conversations. Computational resources were provided by the Livermore High-Performance Computing Center at Lawrence Livermore National Lab (LLNL).

#### References

- [1] S. Pirozzoli, Numerical methods for high-speed flows, *Ann. Rev. Fluid Mech.* 43 (2011) 163–194.
- [2] J. von Neumann, R.D. Richtmyer, A method for the numerical calculations of hydrodynamical shocks, *J. Appl. Phys.* 21 (1950) 232–237.
- [3] A. Jameson, W. Schmidt, E. Turkel, Numerical solution of the Euler equations by finite volume methods using Runge–Kutta time-stepping schemes, in: AIAA Paper 1981-1251 AIAA 5th Computational Fluid Dynamics Conference, 1981.
- [4] A. Cook, W. Cabot, Hyperviscosity for shock-turbulence interactions, *J. Comput. Phys.* 203 (2005) 379–385.
- [5] A.W. Cook, Artificial fluid properties for large-eddy simulation of compressible turbulent mixing, *Phys. Fluids* 19 (2007) 055103.
- [6] S. Kawai, S.K. Lele, Localized artificial diffusivity scheme for discontinuity capturing on curvilinear meshes, *J. Comput. Phys.* 227 (2008) 9498–9526.
- [7] A. Mani, J. Larsson, P. Moin, Suitability for artificial bulk viscosity for large-eddy simulation of turbulent flows with shocks, *J. Comput. Phys.* 228 (2009) 7368–7374.
- [8] F. Ducros, V. Ferrand, F. Nicoud, C. Weber, D. Darracq, C. Gachereau, T. Poinsot, Large-eddy simulation of the shock/turbulence interaction, *J. Comput. Phys.* 152 (1999) 517–549.
- [9] A. Bhagatwala, S.K. Lele, A modified artificial viscosity approach for compressible turbulence simulations, *J. Comput. Phys.* 228 (2009) 4965–4969.
- [10] S. Kawai, S.K. Shankar, S.K. Lele, Assessment of localized artificial diffusivity scheme for large-eddy simulation of compressible turbulent flows, *J. Comput. Phys.* 229 (2010) 1739–1762.
- [11] B. Morgan, S. Kawai, S. Lele, Large-eddy simulation of an oblique shock impinging on a turbulent boundary layer, *AIAA Journal* 2010-4467 (2010).
- [12] S.K. Shankar, S. Kawai, S.K. Lele, Two-dimensional viscous flow simulation of a shock accelerated heavy gas cylinder, *Phys. Fluids* 23 (2011) 024102.
- [13] B.J. Olson, S.K. Lele, Large-eddy simulation of an over-expanded planar nozzle, *AIAA 2011-3908* (2011).
- [14] D.M. Dawson, S. Kawai, S.K. Lele, Large-eddy simulation of Mach 2.9 turbulent boundary layer over a 24 compression ramp, *AIAA 2011-3431* (2011).
- [15] E. Johnsen, J. Larsson, A.V. Bhagatwala, W.H. Cabot, P. Moin, B.J. Olson, P.S. Rawat, S.K. Shankar, B. Sjögren, H. Yee, X. Zhong, S.K. Lele, Assessment of high-resolution methods for numerical simulations of compressible turbulence with shock waves, *J. Comput. Phys.* 229 (2010) 1213–1237.
- [16] S. Kawai, S.K. Lele, Large-eddy simulation of jet mixing in supersonic crossflows, *AIAA J.* 48 (2010) 2063–2083.
- [17] K.J. Franko, R. Bhaskaran, S.K. Lele, Direct numerical simulation of transition and heat-transfer overshoot in a Mach 6 flat plate boundary layer, *AIAA 2011-3874* (2011).
- [18] J.C. Tannehill, D.A. Anderson, R.H. Pletcher, *Computational Fluid Mechanics and Heat Transfer*, Taylor and Francis, 1997.
- [19] S.K. Lele, Compact finite-difference schemes with spectral-like resolution, *J. Comput. Phys.* 103 (1992) 16–42.
- [20] C. Kennedy, M. Carpenter, R. Lewis, Low-storage, explicit Runge–Kutta schemes for the compressible Navier–Stokes equations, *Appl. Numer. Math.* 35 (2000) 177.
- [21] G.S. Jiang, C.W. Shu, Efficient implementation of weighted ENO schemes, *J. Comput. Phys.* 126 (1996) 202–228.
- [22] E. Katzer, On the length scales of laminar shock/boundary layer interaction, *J. Fluid Mech.* 206 (1989) 477–496.
- [23] R.J. Hakkinen, I. Greber, L. Trilling, S.S. Abarbanel, The interaction of an oblique shock wave with a laminar boundary layer, *NASA Memo 2-18-59W* (1959).
- [24] S. Pirozzoli, M. Bernardini, F. Grasso, Direct numerical simulation of transonic shock/boundary layer interaction under conditions of incipient separation, *J. Fluid Mech.* 657 (2010) 361–393.
- [25] M. Klein, A. Sadiki, J. Janicka, A digital filter based generation of inflow data for spatially developing direct numerical or large eddy simulations, *J. Comput. Phys.* 186 (2003) 652–665.
- [26] B.J. Olson, S.K. Lele, Low frequency unsteadiness in nozzle flow separation, *AIAA 2012-2974* (2012).
- [27] D. Papamoschou, A. Zill, A. Johnson, Supersonic flow separation in planar nozzles, *Shock Waves* 19 (2009) 171–183.
- [28] A.D. Johnson, D. Papamoschou, Instability of shock-induced nozzle flow separation, *Phys. Fluids* 22 (2010) 016102.
- [29] H.Y.W. Wong, Overview of flow oscillations in transonic and supersonic nozzles, *J. Propul. Power* 22 (4) (2006) 705–720.
- [30] J. Jeong, F. Hussain, On the identification of a vortex, *J. Fluid Mech.* 285 (1995) 69–94.
- [31] F. Delcayre, Y. Dubief, On coherent-vortex identification in turbulence, *J. Turbul.* 1 (11) (2000) 1–22.